Universiteit Utrecht

Master Internship Thesis

Crystallization of nanoparticles with square-shoulder interactions

July 12, 2017

Author:
A.L. Gabriëlse
3279456

Supervisor:
Prof. Dr. Hartmut Löwen

Daily supervisor:
Dr. Frank Smallenburg

UU supervisor:
Dr. Laura Filion

Acknowledgments

First and foremost, I have to thank my daily supervisor, Frank Smallenburg for his everyday assistance and dedicated involvement in the simulations, writing and presentation. I also would like to thank Laura Filion for bringing me in contact with Frank and making this project possible. And finally Hartmut Löwen for giving me the opportunity to do this internship at the Heinrich Heine University in Düsseldorf.

Abstract

Complex structures in colloidal systems are often stabilized by a competition between different length scales. Inspired by recent experiments on nanoparticles coated with polymers [1, 2], we use Monte Carlo simulations to explore the types of crystal structures that can form in a simple (square shoulder) model which explicitly incorporates two favored distances between the particles. To this end, we implement a Monte Carlo-based crystal structure finding algorithm, following Ref. [3], and use it to explore the types of crystal structure we may expect this system to form, as a function of the interaction range and strength. The aim is to identify sets of interaction parameters where complex crystal structures (such as the C14 lattice observed in Ref. [2]) can be expected to form. Although we do not observe the C14 lattice in this model, a range of new crystal structures are classified. We use cell theory to calculate the free energy of the obtained structures and predict phase diagrams for different interaction ranges.

Contents

1 Introduction

Many everyday substances, such as milk, paint, and ink, contain colloids, particles in the size range between 1 nm and 1 μm. In a colloidal system the colloids are dispersed in a solvent where they constantly collide with the smaller particles of the solvent. Due to these random collisions the colloids move along random trajectories , a behavior known as Brownian motion. This process was named after Robert Brown, who observed this random motion in 1827 studying pollen grains suspended in water under a microscope [4]. Although any object will perform Brownian motion when suspended in a gas or liquid, particles larger then a few micrometer will not significantly be affected by these weak forces. Particles in the colloidal regime, on the other hand, are continually in motion driven by the thermal fluctuations of the solvent. Due to the Brownian motion, colloids can explore their environment, and in that way find structures of low free energy. As the colloids also interact with each other, they show phase behavior analogous to that of atomic and molecular systems. These interactions can lead to the formation of a large range of different structures. Specifically, colloids have been found to self-assemble into gas, liquids and crystals. Additionally, colloids with more complex interactions have been shown to form a variety of liquid crystalline phases [5], out-of-equilibrium phases such as glasses [6] and gels [7], and even quasicrystals [8].

Advances in the synthesis of colloids and nanoparticles (NPs) provide routes to the self-assembly of new complex structures. The understanding and creation of these new experimental systems are helped by theoretical concepts and computer simulations. In particular, the self-assembly of NPs into complex structures can often be understood with fairly simple interactions [9, 10]. An intriguing example of self-assembled complex structures was recently found in gold NPs with a polymer corona, where body centered cubic (BCC) [1], and an even more complex structure known as $MgZn_2$, also labeled $C14$, were observed (Fig. 1.1a) [2]. $MgZn_2$ is a highly complex structure, with a large unit cell. Such a structure is normally not expected to found in single-component systems. The unit cell and hexagonal plane of $MgZn_2$ are depicted in Fig. 1.1c. To better understand how these structures are formed we need to closely examine the interactions between these particles.

A possible explanation for the complex structures formed by the NPs is given by the interactions of the polymers on their surface. In particular, based on experimental observation, it appears that these polymer coatings give rise to two favored length scales for the distance between neighboring particles. This can be explained as state where the polymers are either inter-penetrating or touching, see Fig. 1.2a for a graphical representation. The state with inter-penetrating polymers sets a minimum separation distance between the particles, and could therefore be described as a hard core with diameter σ. Additionally, if the polymers partially interdigitate, they lose a certain amount of entropy, thus making these states less preferred compared to larger separations. This leads to a soft effective potential with a larger interaction range $\sigma + \delta$.

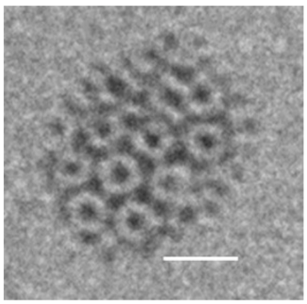

(a) Cryo-TEM image of hydrophobically coated gold NPs (white scale bar, 10 nm).

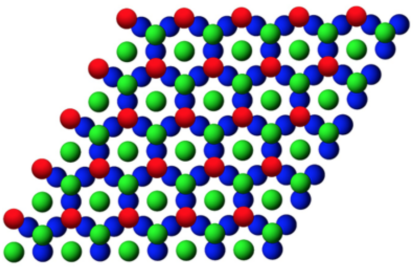

(b) Slice of the $MgZn_2$ ($C14$) structure with a hexagonal plane.

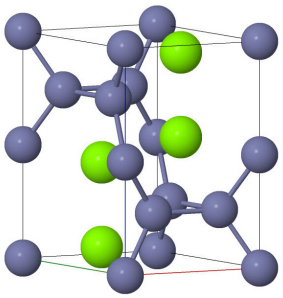

(c) Unit cell of $MgZn_2$ ($C14$) structure. Green spheres indicate the Mg atoms.

Figure 1.1

The main goal of this thesis is to determine if the experimentally observed phase behavior can be explained using a simple model with two length scales. For this, we start off with the simplest possible model: the square shoulder model. Particles with a square shoulder potential interact as a hard core with diameter σ and a soft repulsion with interaction potential ϵ and length δ, see Fig. 1.2b. Although we do not expect the square shoulder potential to be quantitatively precise, it is a good starting point for exploring the minimum requirements for stabilizing the experimentally observed $MgZn_2$ structure.

Despite its simplicity, the square shoulder potential shows a wide variety of phase behavior. Square shoulder potentials have been studied extensively in the range of shoulder length $\delta/\sigma \in \{0.03, .., 0.08\}$ in which an isostructural transition between two FCC structures occurs [11]. At longer shoulder lengths, particles self-assemble in highly complex, low-symmetry lattices, thereby forming clusters, columns, or lamellae [12]. More recently, longer shoulder lengths in two dimensions even have been shown to form quasi-crystalline phases [13].

Here we are interested in the stability of the experimentally observed $MgZn_2$ structure, and of any competing crystal phases. From the observations in [2] we estimate $MgZn_2$ to be favored for a shoulder length in the range $\delta/\sigma \in \{0.15, 0.20\}$. In 1997 a phase diagram was predicted using density-functional theory [14] for $\delta/\sigma = 0.16$. In a more recent study the phase diagram was predicted, for a smoothened potential with $\delta/\sigma = 0.15$, using thermodynamic integration to an Einstein crystal. For $\delta/\sigma = 0.20$ a phase diagram was predicted in Ref. [15] where the authors predict both a stable BCC structure and a significantly more complex $A15$ lattice. However, in these studies the $MgZn_2$ structure was not taken into account, nor was a systematic search conducted for alternate stable crystal structures. Additionally, in Ref. [15] the effects of temperature on the stability of the fluid were neglected. In light of the new experimental observations of Ref. [1, 2], we revisit this phase diagram in more detail, and explore the stability of the fluid phase as well as a number of competing crystal phases. In order to do this, we systematically predict candidate crystal structures using a crystal structure prediction method based on Monte Carlo simulations [3]. For the predicted crystal structures we use free energy calculations to predict their stability in a phase diagram.

The thesis is organized as follows. In Sec. 2 we describe the methods we use to simulate the crystal structures and to calculate an approximate free energy of the found structures. Furthermore, in this section we provide a method to calculate the free energy of fluid phase. The results are presented in Sec. 3, where we reexamine the phase-behavior of the square shoulder interaction for shoulder lengths $\delta/\sigma \in \{0.15, 0.20\}$. The thesis is concluded in Sec. 4.

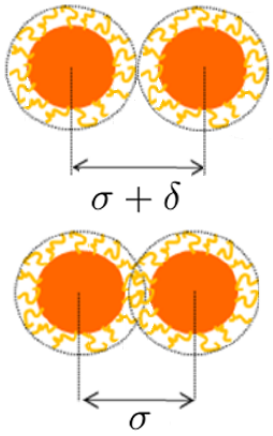

(a) Representation of polymer coated NPs. Two different interaction lengths σ for inter-penetrating polymers and $\sigma + \delta$ touching polymers.

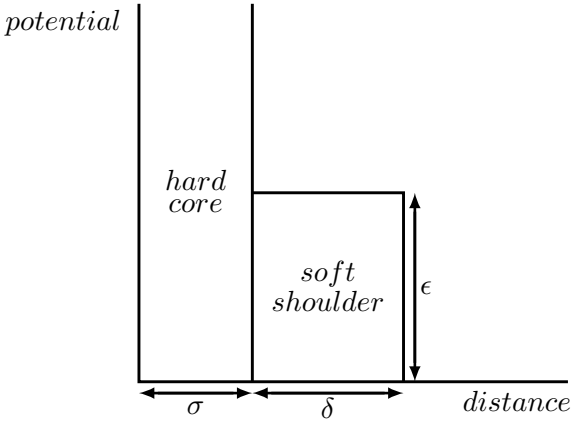

(b) Square shoulder potential. Hard core with diameter σ and a soft shoulder with potential ϵ and shoulder length δ.

Figure 1.2

2 Methods

In this thesis, we employ Monte Carlo methods to simulate the self-assembly of particles with square shoulder interactions. In these simulations we fix the number of particles N, pressure P and temperature T, the isobaric-isothermal NPT-ensemble. Possible candidate crystal structures are predicted using the floppy box Monte Carlo method. To determine the stability of these structures we use free energy calculations based on mean field theory. The free energy of the fluid phase is calculated by thermodynamic integration of the fluid equation of state. In the following subsections we describe these methods in more details.

2.1 Metropolis Monte Carlo Simulations

To simulate the crystal behavior of colloidal particles we use the Monte Carlo (MC) method. The MC method is based on random sampling to obtain numerical results. Consider the canonical ensemble where the number of particles N, the volume V and the temperature T are fixed. The Hamiltonian describing this system is given by

$$H(\mathbf{r}^N, \mathbf{p}^N) = \sum_{i=1}^{N} \frac{\mathbf{p}_i^2}{2m} + U(\mathbf{r}^N), \tag{2.1}$$

with the momenta $\mathbf{p}^N$ of the particles and the potential U, depending on the positions $\mathbf{r}^N$ of these particles. For this system the canonical partition function is given by

$$Z(N, V, T) = \frac{c}{N!} \int d\mathbf{r}^N \exp(-\beta U(\mathbf{r}^N)), \tag{2.2}$$

where $\beta = 1/k_B T$ with Boltzmann constant k_b and c a normalization constant resulting from integrating over the momenta. We can now express the average of a momentum-independent observable O as

$$\langle O \rangle = \frac{\int d\mathbf{r}^N O(\mathbf{r}^N) \exp(-\beta U(\mathbf{r}^N))}{\int d\mathbf{r}^N \exp(-\beta U(\mathbf{r}^N))}. \tag{2.3}$$

Because we can not easily calculate the integral over the whole phase space, we use the MC method. Instead of integrating over the entire phase space we consider a set of n configurations $\mathbf{r}_1^N, \mathbf{r}_2^N, ..., \mathbf{r}_n^N$. For n random configurations, a Markov chain, the ensemble average would be

$$\langle O \rangle = \frac{\sum_{i=1}^{n} O(\mathbf{r}_i^N) \exp(-\beta U(\mathbf{r}_i^N))}{\sum_{i=1}^{n} \exp(-\beta U(\mathbf{r}_i^N))}. \tag{2.4}$$

In a Metropolis sampling algorithm [16] we generate $\mathbf{r}_i^N$ so that the probability of generating $\mathbf{r}_i^N$ is proportional to $\exp[-\beta U(\mathbf{r}_i^N)]$. The ensemble average reduces to

$$\langle O \rangle = \frac{\sum_{i=1}^{n} O(\mathbf{r}_i^N)}{n}. \tag{2.5}$$

The algorithm starts with an initial configuration $\mathbf{r}_{init}^N$ and computes a trial configuration $\mathbf{r}_{trial}^N$ where, for example, a random particle is moved. The new trial configuration is accepted with probability

$$acc(init \to trial) = min(1, \exp\{-\beta[U(\mathbf{r}_{trial}^N) - U(\mathbf{r}_{init}^N)]\}) \tag{2.6}$$

The initial configuration is kept if the move is rejected. Otherwise the trial move becomes the new initial configuration. By repeating these steps many times the system will reach an equilibrium from which the average observable can be calculated.

2.2 Isobaric-Isothermal Ensemble

In the previous section we described the Metropolis Monte Carlo method in a canonical or NVT ensemble. It is sometimes convenient to fix the pressure P instead of the density, specifying a pressure is usually easier. Therefore, in this report, we mainly use the isobaric-isothermal NPT ensemble. In the NPT ensemble additional steps are performed to change the volume V of the system. A trial volume change consists of an increase or decrease in the box size in which all particles are scaled accordantly. Trial moves are now accepted with probability

$$acc(init \to trial) = min(1, (V_{trial}/V_{init})^N \exp\{-\beta P[V_{trial} - V_{init}] - \beta[U(\mathbf{r}^N_{trial}) - U(\mathbf{r}^N_{init})]\}). \tag{2.7}$$

To perform our simulation we need to define the potential between particles. The square shoulder potential between a pair of spherical particles can be written as,

$$U(r) = \begin{cases} \infty & r < \sigma \\ \epsilon & \sigma < r < \sigma + \delta \\ 0 & r > \sigma + \delta \end{cases}$$

Where r is the distance between the particle centers, σ the diameter of the particle and ϵ the potential of the shoulder with length δ.

2.3 Floppy Box Monte Carlo

An effective method for crystal structure prediction of colloidal particles is the floppy-box Monte Carlo (FBMC) method [3]. Floppy-box simulations are based on the Monte Carlo method, as described in Sec. 2.1, in the isobaric-isothermal ensemble, Sec. 2.2. The main goal is to find the unit cell of a crystal. Therefore, to obtain crystal structures efficiently in a floppy-box simulation the number of particles is small, $N \lesssim 15$. This allows for rapid sampling of different crystal structures. For the simulation box to act as unit cell we let the three vectors, which span the simulation box, vary separately both in length and orientation. Crystal structure prediction then proceeds via a slow compression from a low density gas or liquid phase to higher densities by increasing the pressure or lowering the temperature. Repeating the floppy-box simulations with different initial configurations will result in a number of favorable crystal configurations which can then be further explored for stability.

As we only simulate the unit cell of a crystal we need to consider interaction with its periodic self images. The number of images determines the computational efficiency of the simulations. Therefore we will need to determine the lowest number of images which checks all contributing interaction pairs. In the next sections we will describe the set up for the floppy-box method as used in this report.

2.3.1 Monte Carlo Moves And Acceptance Rules

Let us consider a simulation box with three box vectors $\mathbf{v}_j$ with, $j = 1, 2, 3$. The vertices of the box are in a standard Cartesian coordinate frame. One of the box vertices is located at the origin of this frame. In the box we consider a set of N particles with positions of their center of rotation located at $\mathbf{r}_i$ where, i indicates particles 1 up to N. As we only consider spherical particles we can neglect the orientation of the particles. The volume of the box is given by $V = |\mathbf{v}_1 \cdot (\mathbf{v}_2 \times \mathbf{v}_3)|$. The energy of the system will depend on the box vectors and the particle positions, $U(\mathbf{v}^3, \mathbf{r}^N)$.

In our FBMC simulations there are three possible types of trial moves: translation of a particle, uniform scaling of all three box vectors and deformation of the box by varying one of the box vectors, as depicted in Fig. 2.1. Each move will be accepted according to Sec. 2.2 in the NPT ensemble. A combination of deformation and scaling of the box will result in a faster equilibration than deformation alone. Each translation move we randomly move a particle in one dimension where the maximum displacement is chosen such that a 35% acceptance rate is achieved. In a uniform box scaling move we rescale each box vector by

a factor which will result in a 15% acceptance rate and in a box deformation move we randomly change a box vector in one dimension with a factor that also results in a 15% acceptance rate.

Since in a FBMC simulation the box vectors are not orthogonal it is more convenient to use a set of scaled coordinates to describe the positions of the particles. Consider $\mathbf{s}_i \in [0,1)^3$, for particle $i = 1, 2, .., N$. These scaled coordinates $\mathbf{s}_i$ can be related to the real space coordinates $\mathbf{r}_i$ via a bijective function $\mathbf{r}_i = M\mathbf{s}_i$, with matrix M constructed from the box vectors: $M = (\mathbf{v}_1, \mathbf{v}_2, \mathbf{v}_3)$. In this scaled coordinate system it is easier to find the periodic images of the box as a periodic image $\mathbf{P}_{im}$ is located an integer from the original position, $P_{im} = \mathbf{s}_i\{i\hat{\mathbf{x}} + j\hat{\mathbf{y}} + k\hat{\mathbf{z}}\}$, with $i, j, k \in \mathbb{Z}$.

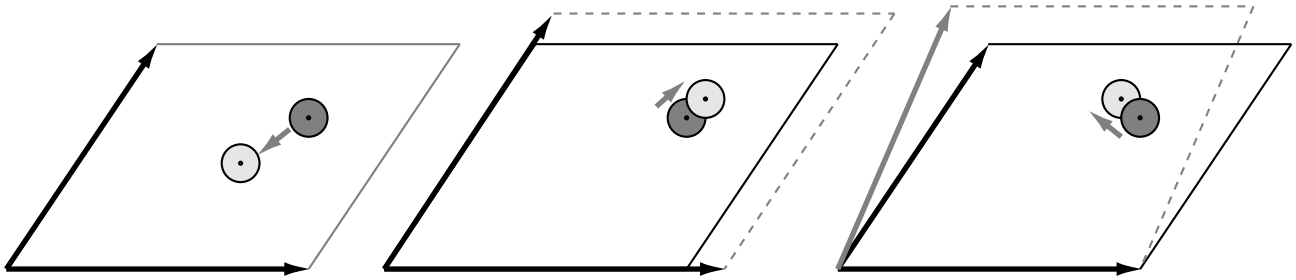

Figure 2.1: Two dimensional representation of FBMC trial moves. Translation of a particle (left), uniform scaling of all box vectors (middle) and box deformation by varying one of the box vectors (right). Light gray indicates a trial move.

2.3.2 Image Lists

As we already mentioned we need an efficient way to determine the number of periodic images to consider for checking all contributing interaction pairs. Here we can consider three types of overlap checks for a particle: overlap with all other particles in the box, overlap with its own periodic images and overlap with other particles' periodic images. To construct a set of images we check all images within a radius $R = 2(\sigma + \delta)$ in real space, as particle pairs separated by larger distances will not interact, here the factor 2 is chosen to make sure all nearest neighbors are considered.

First we construct an image list for each particles own periodic images. The center of this particle will be the origin. We then select a plane through the origin and orthogonal to the vector $\mathbf{v}_1 + \mathbf{v}_2 + \mathbf{v}_3$. Due to the symmetric properties of the unit cell we only have to consider images at one side of this plane, see Fig. 2.2. A large enough image list can be realized by considering a cube with vertices at $\mathbf{c}_n = R(\pm\hat{\mathbf{x}} \pm \hat{\mathbf{y}} \pm \hat{\mathbf{z}})$, with $n = 1, .., 8$ vertices and $\hat{\mathbf{x}}, \hat{\mathbf{y}}, \hat{\mathbf{z}}$ Cartesian unit vectors.

Applying the inverse matrix of M, $\mathbf{p}_n = M^{-1}\mathbf{c}_n$ will result in a parallelepiped in the scaled coordinate system. The upper bound of $\mathbf{p}_n$ in each direction can be found by

$$\begin{aligned} N_1 &= \lceil \max_n(\mathbf{p}_n \cdot \hat{\mathbf{x}}) \rceil, \\ N_2 &= \lceil \max_n(\mathbf{p}_n \cdot \hat{\mathbf{y}}) \rceil, \\ N_3 &= \lceil \max_n(\mathbf{p}_n \cdot \hat{\mathbf{z}}) \rceil. \end{aligned} \tag{2.8}$$

Here $\lceil \cdot \rceil$ is the round up resulting in the highest integer of $\mathbf{p}_n$ in each dimension. The resulting images in the scaled coordinate system are $P_{im} = \{i\hat{\mathbf{x}} + j\hat{\mathbf{y}} + k\hat{\mathbf{z}}\}$, with $i = 0, .., N_1$, due to symmetry; $j = -N_2, .., N_2$; $k = -N_3, .., N_3$. An image list for images of other particles can simply be constructed by adding another layer to the image list of the self images. For every volume move we need to recalculate the image list of the system.

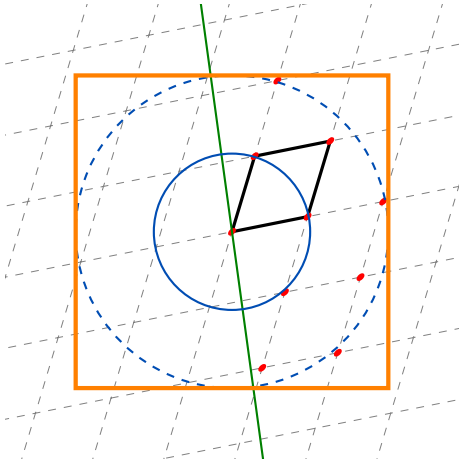

Figure 2.2: Constructing image list for a particles own periodic images. Red dots indicate periodic images of the particle within a box (orange rectangle) around the sphere with radius R (blue dashed circle). We only consider one side of the plane (green line) due to symmetric properties of the unit cell.

2.3.3 Lattice reduction

In a FBMC simulation the deformation of the box could lead to extreme distortions where the box becomes very flat of elongated. In this case, the angles between the box vectors will become very large or small. As a result the image-lists become very large, reducing the efficiency of the simulations. To reduce the flatness of the box we implement a lattice reduction algorithm. In a lattice reduction algorithm the basis vectors are replaced by a combination of these vectors which are shorter and more orthogonal. The distortion D of the box is defined by the surface-to-volume ratio

$$D(\mathbf{v}_1, \mathbf{v}_2, \mathbf{v}_3) = \frac{1}{9}(|\mathbf{v}_1| + |\mathbf{v}_2| + |\mathbf{v}_3|) \cdot \frac{|\mathbf{v}_1 \times \mathbf{v}_2| + |\mathbf{v}_1 \times \mathbf{v}_3| + |\mathbf{v}_2 \times \mathbf{v}_3|}{\mathbf{v}_1 \cdot (\mathbf{v}_2 \times \mathbf{v}_3)} \tag{2.9}$$

with the norm of the vector indicated by $|\cdot|$. Here we multiply the average box vector length with the area of the box and dividing by the box volume. The distortion is normalized such that $D = 1$ equals a cube. We only perform a lattice reduction if $D > 1.5$, indicating a significantly distorted box. If $D > 1.5$ we calculate a set of 12 vector combinations

$$\begin{aligned} &\{\mathbf{v}_1 \pm \mathbf{v}_2, \mathbf{v}_2, \mathbf{v}_3\}, \{\mathbf{v}_1 \pm \mathbf{v}_3, \mathbf{v}_2, \mathbf{v}_3\} \\ &\{\mathbf{v}_1, \mathbf{v}_2 \pm \mathbf{v}_1, \mathbf{v}_3\}, \{\mathbf{v}_1, \mathbf{v}_2 \pm \mathbf{v}_3, \mathbf{v}_3\} \\ &\{\mathbf{v}_1, \mathbf{v}_2, \mathbf{v}_3 \pm \mathbf{v}_2\}, \{\mathbf{v}_1, \mathbf{v}_2, \mathbf{v}_3 \pm \mathbf{v}_3\}. \end{aligned} \tag{2.10}$$

For each of these combinations we calculate the surface area of the box and use the one with the smallest surface area. For this new set of vectors we again calculate 12 new combinations and repeat this process until there is no longer a set with a smaller surface area. The particles are then placed back in the box spanned by this set of more orthogonal vectors. A two dimensional representation is shown in Fig. 2.3.

2.3.4 Total energy

For the square shoulder model it is important to keep track op the total energy of the system. We should be aware that we do not double count the pair-potential between particles. If two particles have a distance between σ and $\sigma + \delta$ we should only add a single pair-potential ϵ to the system. To make sure that the total energy stays correct throughout the simulations we calculate the total energy of the system every 100 cycles and confirm that updated energy matches the new total energy.

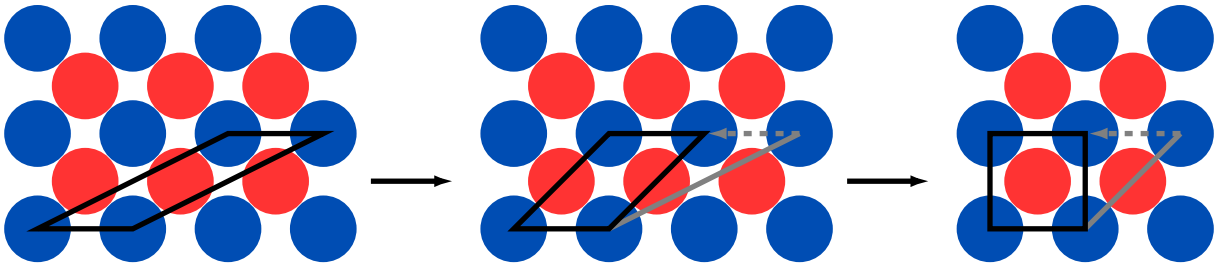

Figure 2.3: Two dimensional representation of a lattice reduction. A crystal with two particles (red and blue) in a unit cell. From left to right the unit cell will become more orthogonal. Here the black lines represent the unit cell and the gray line indicates the reduced vector. Particle positions in real space do not change.

2.4 Free energy calculations

In this section we will describe the free energy for a system with a square shoulder potential. For this we will first describe the free energy of the fluid phase by expanding the ideal gas law with the second virial coefficient and integrating the resulting equation of state. The free energy of a solid (crystal) phase can be calculated using mean field theory.

2.4.1 Second virial coefficient

A common method for the study of the Helmholtz free energy F of a fluid is thermodynamic integration [17] of the equation of state P as function of the density ρ

$$\frac{\beta F(\rho)}{N} = \frac{\beta F_{id}(\rho)}{N} + \int_0^\rho d\rho' \frac{\beta P(\rho') - \rho'}{\rho'^2} \tag{2.11}$$

where $F_{id}(\rho) = Nk_bT(\log \rho\Lambda^3 - 1)$ corresponds to the free energy of an ideal gas for N particles and thermal wavelength Λ. At low densities a fluid behaves as an ideal gas. We can expand the ideal gas law by a so-called virial expansion to approximate the equation of state at higher densities. In particular, we can express the pressure p as a function of the temperature T and density ρ

$$p(\rho, T) = k_bT(\rho + B_2(T)\rho^2 + B_3\rho^3 + ..), \tag{2.12}$$

with k_b the Boltzmann constant. The temperature dependent virial coefficients $B_n(T)$ can be calculated by fitting the equation of state obtained from, e.g. low density simulations. Alternatively, we calculate an explicit expression for the second virial coefficient $B_2(T)$ in terms of the pairwise square shoulder potential. For an isotropic interaction potential:

$$B_2 = -\frac{1}{2}\int 4\pi f(r) r^2 dr. \tag{2.13}$$

Here $f(r) = \exp(-\beta U(r)) - 1$, with $\beta = 1/k_bT$ and $U(r)$ the square shoulder potential defined as

$$U(r) = \begin{cases} \infty & r < \sigma \\ \epsilon & \sigma < r < \sigma + \delta \\ 0 & r > \sigma + \delta \end{cases}.$$

The resulting second virial coefficient as a function of potential ϵ and shoulder length δ is given by

$$B_2 = -\frac{2\pi}{3}(\sigma + \delta)^3(e^{-\beta\epsilon} - 1) + \frac{2\pi}{3}\sigma^3 e^{-\beta\epsilon}. \tag{2.14}$$

We obtain higher order coefficients by fitting the equations of state.

2.4.2 Cell theory

A simple method to approximately calculate the free energy of a crystal to use mean field theory. For the free energy in a crystal let us consider a single particle in a periodic lattice. All other particles are fixed at these lattice positions. We can calculate the average free energy of a particle in the crystal by inserting this particle randomly at different positions in a approximate volume in which the center of the particle could move, see Fig. 2.4 for a two dimensional representation. For each insertion we calculate the total energy of the particle with the square shoulder potential to obtain the single particle partition function [18, 19]

$$Q = \frac{V_0}{\Lambda^3} \left\langle \exp\left(-\beta \left[u(\mathbf{r}) - \frac{1}{2}u(\mathbf{r}_0)\right]\right)\right\rangle_{V_0}, \tag{2.15}$$

where u is the energy of a single particle at position $\mathbf{r}$ and $\mathbf{r}_0$ the position of the particle in the lattice. The free energy per particle can be calculated from the partition function Q as

$$\frac{\beta F}{N} = -\ln(Q) \tag{2.16}$$

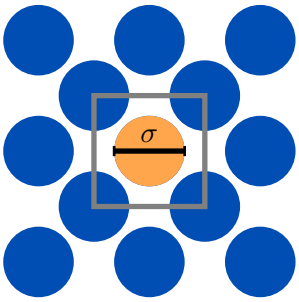

Figure 2.4: Two dimensional representation of cell theory. A crystal with particles (blue) at fixed lattice positions and a selected particle (orange) which is randomly inserted within an area (gray box).

The total free energy will result from repeating these steps for each particle in the system. The volume in which the particle is inserted should be chosen carefully, a to small volume will result in a lower free energy. In the special case where the particles are close-packed, all injections will lead to an overlap. As a result, the partition function will be zero and therefore have an undefined free energy. Consequently, the free energy asymptotically diverges as it approaches close packing.

3 Results

In this section we will present our results on the crystal structures for spheres with a square shoulder potential. The floppy-box Monte Carlo (FBMC) method, as described in Sec. 2.3, will provide potential candidate structures. The stability of these candidate structures will be tested with free energy calculations using cell theory, as described in Sec. 2.4.2.

3.1 Floppy-box simulations

At finite temperatures we can use FBMC simulations to predict the crystal structures of colloidal particles. Here we will present the results obtained for simulations on colloidal spheres with a square shoulder potential

$$U(r) = \begin{cases} \infty & r < \sigma \\ \epsilon & \sigma < r < \sigma + \delta \\ 0 & r > \sigma + \delta \end{cases}.$$

As we mentioned in the introduction we are interested in range of the shoulder length $\delta/\sigma = \{0.15, 0.20\}$ for different potentials ϵ. In the FBMC simulations we keep $P\sigma^3/\epsilon$ constant and slowly decrease the temperature from $\beta\epsilon = 1$ to $\beta\epsilon = 10$. We then continue the simulations with a temperature of $\beta\epsilon = 1000$ to suppress thermal fluctuations in the final configuration.

For every combination of pressure and temperature the structure, or structures, of the system will favor the lowest possible Gibbs free energy $G = U - TS + PV$, where U is the internal energy, T the temperature, S the entropy P the pressure and V the volume of the system. In the limit that $T \to 0$, a combination of the internal energy and density will determine the stability of a structure. The contribution of the density is determined by the pressure. For structures with the same energy U the system will prefer a structure with the highest density.

To verify that our FBMC algorithm works we start by predicting the crystal structure for $\beta\epsilon = 0$ which is simply a hard sphere system were the only important parameter is $\beta P\sigma^3$. It is well known that, at high pressures, the system will favor the face centered crystal (FCC) structure. In a floppy-box, the unit cell contains only a single particle $N = 1$. The initial configuration of the system will be in a low density fluid-phase. In Fig. 3.1 we present snapshots of a crystal obtained from a FBMC simulation with pressure $\beta P\sigma^3 = 4000$. Although a trained eye might recognize the structure of this system to be FCC, a set of parameters should be used to verify its structure. The first indication that this could indeed be an FCC structure is the resulting packing fraction $\eta \approx 0.7402$ as the packing fraction of a close packed FCC structure is $\pi/3\sqrt{2} \approx 0.7404$. To quantitatively measure the structure of the system we use three-dimensional bond order parameters provided from spherical harmonics. These order parameters quantify the symmetry of the neighborhood around each particle in the crystal, such that direct comparisons with known structures can be made. We consider four different parameters: Q4, Q6, W4, and W6, as described in [20], which we calculate using a slightly modified version of the code provided in [21]. For FCC, HCP, BCC and liquid phases the parameters are shown in Table 1. The parameters obtained for the crystal shown in Fig. 3.1 match the parameters for FCC, as shown in Table 1. From this we can conclude that our FBMC method works for hard spheres ($\beta\epsilon = 0$).

Table 1: Bond parameters, Q4, Q6, W4 and W6 for FCC, HCP and fluid, data from [21], BCC added with data from [22]. The last row contains the parameters obtained from the FBMC simulation. These match the data for FCC.

	Q4	Q6	W4	W6
FCC	0.19094	0.57452	-0.159317	-0.013161
HCP	0.09722	0.48476	0.134097	-0.012442
BCC	0.036	0.511	0.159	0.013
Fluid	0	0	0	0
Simulated	0.190941	0.574524	-0.159317	-0.0131606

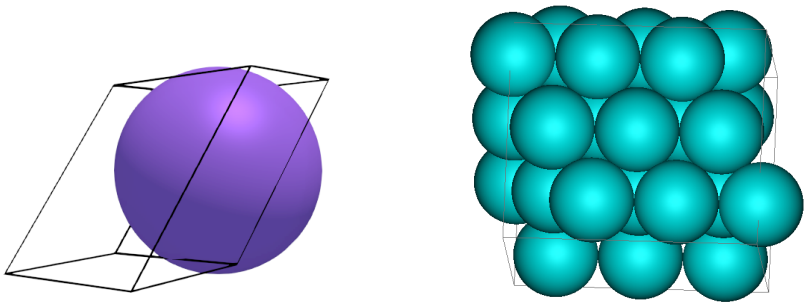

(a) Floppy box unit cell.

(b) Periodic structure

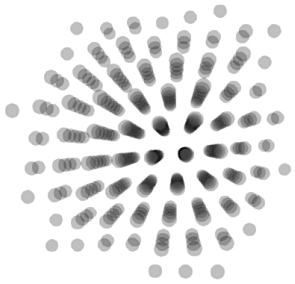

(c) Periodic structure as point particles.

Figure 3.1: Snapshots of FBMC simulations on hard spheres ($\beta\epsilon = 0$). A single particle simulated at pressure $\beta P\sigma^3 = 4000$. Snapshots provided for the resulting unit cell of the floppy box (**a**), a periodic structure of this unit box (**b**) and periodic structure of point particles to provide more insight in the structure (**c**).

Now that we have verified the FBMC method we can run a series of simulations to obtain the low temperature crystal structures with a square shoulder potential. As we do not know how many particles a unit cell could contain we will simulate possible unit cells with $N \in \{2, 3, 4, 5, 6, 8, 10, 12, 14\}$ particles. For each N we will simulate square shoulder potentials $\beta\epsilon \in \{0.25, .., 2.00\}$, with increasing steps of 0.25, for shoulder length $\delta/\sigma \in \{0.15, 0.20\}$. For each of these combinations we set the pressure of the system to $\beta P \in \{2, ..., 20\}$ with increasing steps of 0.5. This results in a total of 640 different combinations of configurations per number of particles N. In Fig. 3.2 the bond parameters are plotted for $N = 2$ and $\delta/\sigma = 0.15$. Here we can observe that there are many different structures. A way to find possible stable candidate crystal structures is to check if there are combinations of parameters which occur often. As we know the bond parameters for both FCC and HCP we first check how often these can be found in this set. There are 28 different configurations that match both the packing fraction and bond order parameters for FCC and 25 that match the HCP parameters. These all have a very small difference and therefore cannot be distinguished in Fig. 3.2. In the results we also observe a large number of structures that match the bond parameters of both FCC (23 times) and HCP (15 times) but with a lower packing fraction. This is the result of the square shoulder potential dominating the pressure. We will call these $FCC + \delta$ and $HCP + \delta$. The resulting packing fraction of these structures are $\eta < \pi/(3\sqrt{2}[(\sigma + \delta)/\sigma]^3) \approx 0.4869$.

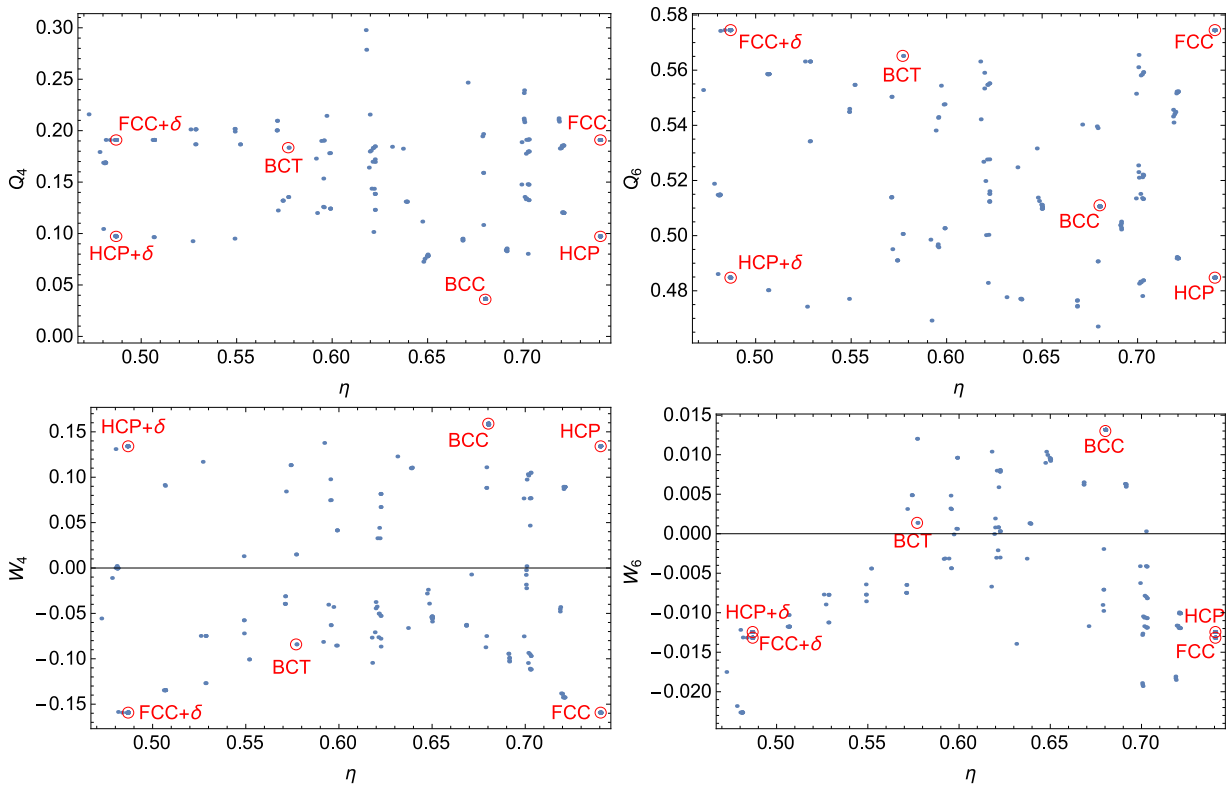

Figure 3.2: Plots of bond parameters Q4, Q6, W4 and W6 for $N = 2$ particles in a unit cell and shoulder length $\delta/\sigma = 0.15$ for different potentials $\beta\epsilon \in \{0.25, ..., 2.0\}$ and pressures $\beta P\sigma^3 \in \{2, 20\}$.

As there are many structures still not identified we will plot each configuration as $E = \beta U/V$ against the packing fraction η, Fig. 3.4. The lowest possible energy for each packing fraction is the lowest point or coexistence between two of these points. In Fig. 3.4a the lowest points are connected resulting in 4 stable configurations at the lower temperature limit for $\delta = 0.15$. We already identified the FCC/HCP and $FCC{+}\delta/HCP{+}\delta$ structures. As both FCC/HCP have the same highest packing fraction and energy they will be indistinguishable and in the top right corner of Fig. 3.4. The highest packing fraction with zero energy will be either $FCC + \delta$ or $HCP + \delta$. As in both hard-sphere and square shoulder systems the FCC phase has been shown to be more stable than HCP [23], we assume in the following that holds in our system as well. In addition to these structures there are still two structures not identified. The first structure has 8 bonds per particle and a packing fraction of $\eta \approx 0.680$, see Fig. 3.3a for a snapshot of the unit cell with nearest neighbors. A body centered crystal BCC structure has 8 bonds per particle and a packing fraction of $\eta = \pi\sqrt{3}/8 \approx 0.68017$. Together with matching order parameters $Q_4 \approx 0.036$ and $Q_6 \approx 0.511$ compared to Table 1 we can conclude that the third stable structure is BCC. The last structure is depicted in Fig. 3.3b. It has 4 bonds per particle and a maximum packing fraction of $\eta \approx 0.577$. This structure is commonly known as body centered tetragonal BCT [24]. In a BCC structure the height a and base c of the unit cell have the same length resulting in a cubic structure. For a BCT structure $a \neq c$, resulting in a rectangular structure with a square base. The 4 resulting bonds are all in a plane, therefore the BCT structure will have layers of particles in a square planar lattice.

Figure 3.3

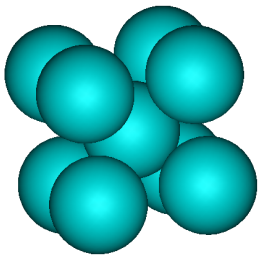

(a) BCC unit cell.

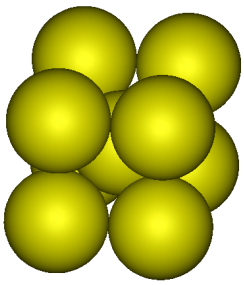

(b) BCT unit cell.

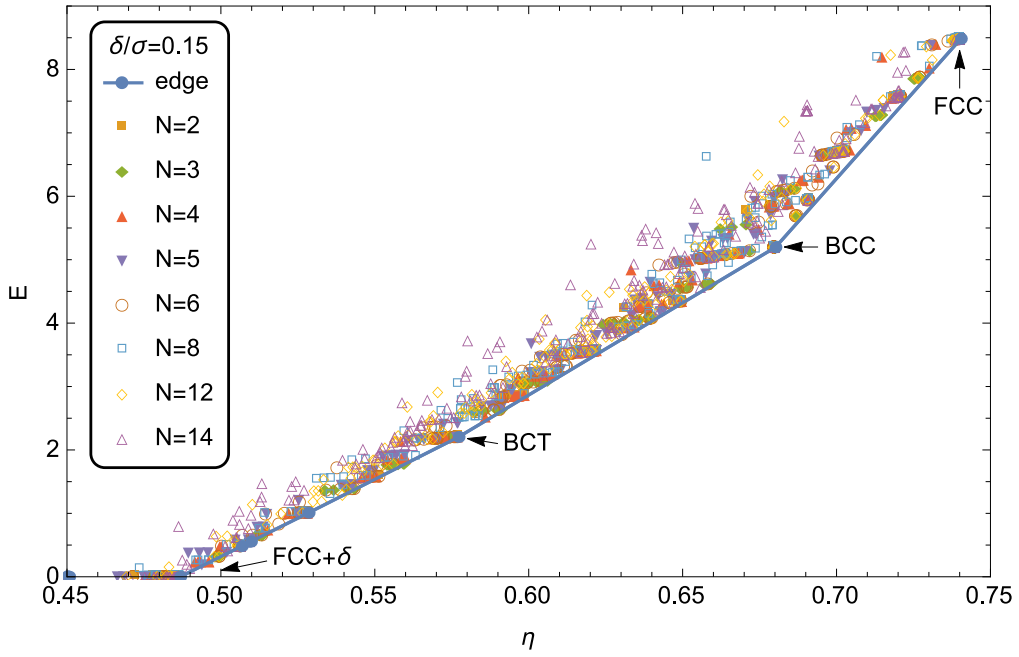

(a)

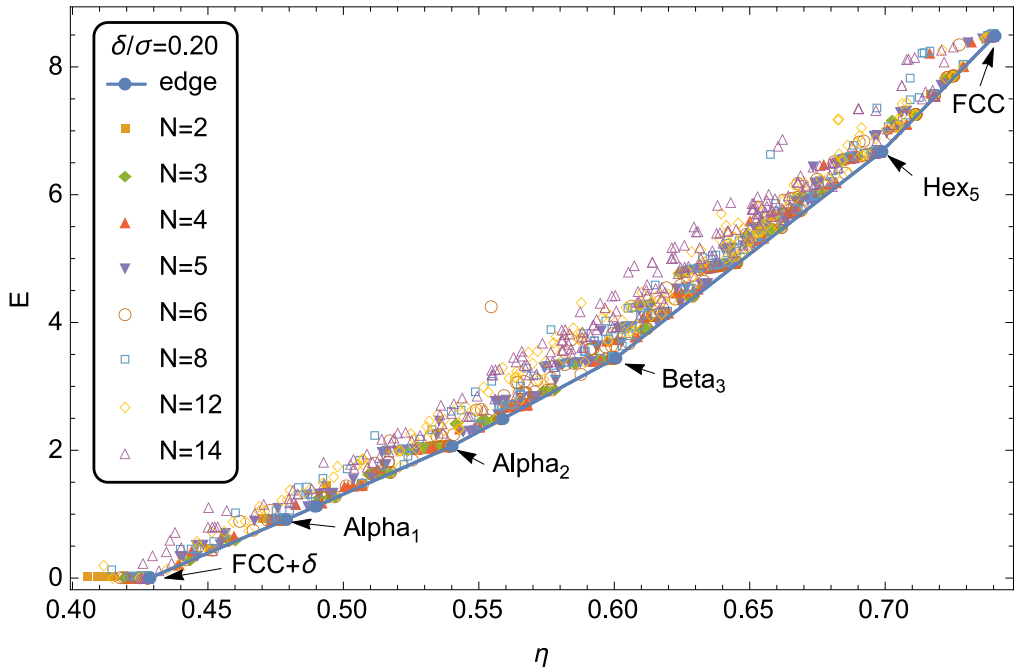

(b)

Figure 3.4: FBMC results plotted as $E = \beta U \sigma^3 / V$ as function of the packing fraction η for square shoulder length $\delta/\sigma = 0.15$ (a) and $\delta/\sigma = 0.20$ (b). Structures with the lowest energy per volume are connected, indicated by the blue line.

As the stable structures found in Fig. 3.4b are not yet classified, besides FCC and $FCC + \delta$, we will classify them by their planar structure and energy contribution. Each structure, like FCC and $FCC + \delta$ consists of hexagonal planes. We can describe the structures by considering an $FCC + \delta$ structure and compressing it in one or more directions. The structure with the lowest density after $FCC + \delta$ has 2 bonds per particle. It consists of a hexagonal plane which is compressed in one direction, see Fig. 3.5a. We will label this as an *Alpha*-plane. Between planes there are no bonds. If we increase the density, the planes are compressed which leads to 2 additional bonds, see Fig. 3.5b. By compressing the hexagonal plane into the opposite direction of the *Alpha*-plane a *Beta*-plane is formed which has 4 bonds in the plane. In Fig. 3.5c we observe that there are 2 bonds between the planes for a total of 6 bonds per particle. By compressing the plane in 2 directions we get an hexagonal plane with 6 bonds, see Fig. 3.5d. The planes are compressed to form 4 bonds for a total of 10 bonds per particle. Note that in our FBMC simulations, we often observe combinations of these crystals, where for example *Alpha*-planes are alternatively stacked with 0 or 1 interplanar bonds. This leads to additions stable points in Fig. 3.4b.

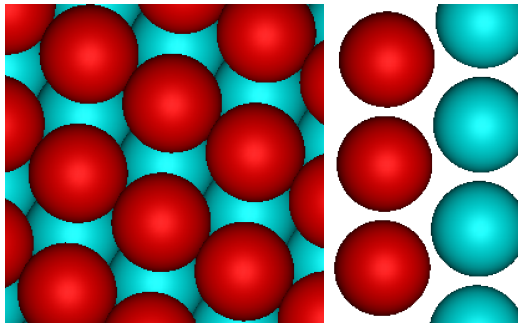

(a) $Alpha_1$, $\eta \approx 0.479$.

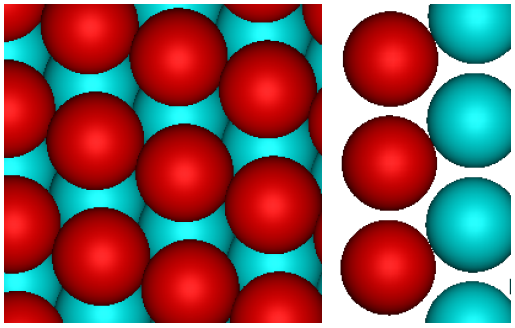

(b) $Alpha_2$, $\eta \approx 0.540$

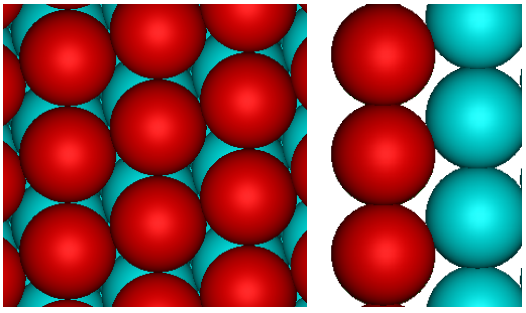

(c) $Beta_3$, $\eta \approx 0.600$.

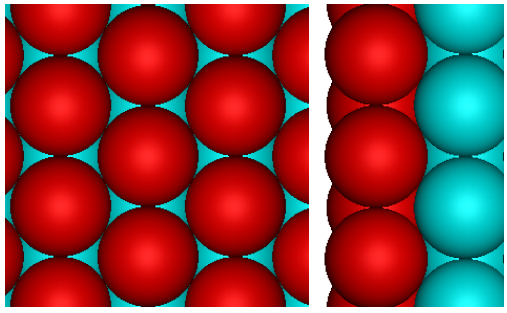

(d) Hex_5, $\eta \approx 0.699$.

Figure 3.5: Graphical representations of stable structures found in Fig. 3.4b. Structures are classified by the planes and the energy contribution per particle. See text for more details on the classification of the planes.

3.2 Free energy

Now that we have discovered potential stable crystal structures in the low temperature limit we can calculate their Helmholtz free energy to establish the range in which they are stable. To fully determine their stability, we also require the free energy of the fluid phase for each temperature. As described in Sec. 2.4.1 we will calculate the free energy by integration of the equation of state.

3.2.1 Equations of state of the fluid phase

To calculate the Helmholtz free energy of the fluid phase with square shoulder potential we start with a low density system of $N = 343$ particles. For each potential $\beta\epsilon \in \{0.25, ..., 5.0\}$ and shoulder length $\delta/\sigma \in \{0.15, 0.20\}$ we perform a simulation in which we slowly increase the pressure at fixed temperature. For each pressure we let the system equilibrate before further increasing the pressure. As the pressure increases the system becomes more dense until it reaches a phase transition to a solid phase. In Fig. 3.6 we plot the equation of state for a system with $\beta\epsilon = 0.25$ and $\delta/\sigma = 0.15$. Here we can clearly see the phase transition around $\rho\sigma^3 \approx 1.05$ due to the jump in density. For the free energy integration we only want to fit the equation of state in the fluid phase. Hence, for each ϵ and δ we discard all points after the phase transition.

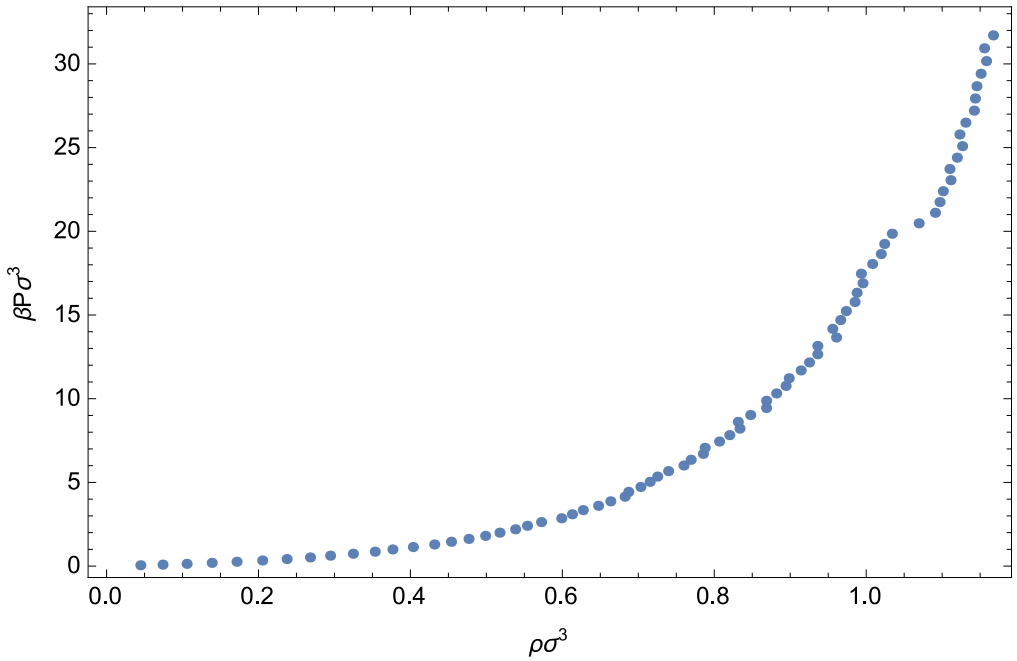

Figure 3.6: Equation of state for square shoulder potential $\beta\epsilon = 0.25$ and shoulder length $\delta/\sigma = 0.15$. The phase transition around $\rho\sigma^3 \approx 1.05$ can be observed by the jump in density.

In figure 3.7 all the equations of state are plotted for $\delta/\sigma = 0.15$. Using these equations of state we can fit an expansion of the ideal gas law as described in Sec. 2.4.1. This results in the fits plotted in Fig. 3.6. For high ϵ the phase transition shifts to lower densities. Therefore, in further calculations we have to make sure that we do not use these fits beyond the range of which we have data for the fluid equation of state. We calculate the free energy as a function of the density for the fluid phase using Eq. 2.11.

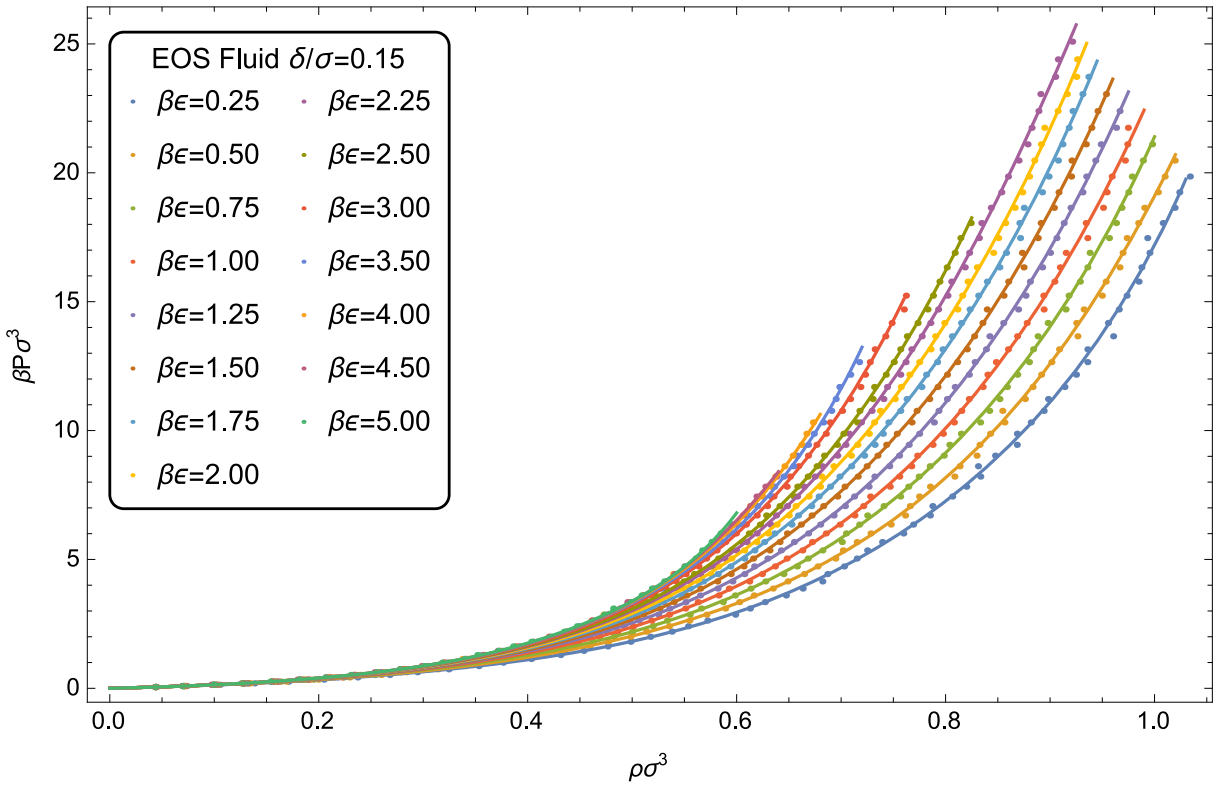

Figure 3.7: Equations of state for square shoulder length $\delta/\sigma = 0.15$ for a range of $\beta\epsilon \in \{0.25, ..., 5.0\}$. Points above the phase transition are discarded as we are only interested in the fluid phase. Colored lines indicate the fits through the corresponding fluid equation of state.

3.2.2 Cell theory

The free energy of crystalline phases can be calculated using cell theory as described in Sec. 2.4.2. We will use cell theory to calculate an approximate free energy for the low temperature limit crystal structures found in the FBMC simulations in Sec. 3.1. To test the stability of the found structures we will calculate the free energy for different potentials $\beta\epsilon \in \{0.5, .., 5.0\}$ with shoulder length $\delta/\sigma \in \{0.15, 0.20\}$ as a function of the density. As the free energy of a close packed system is infinitely large we start the calculations with densities close to the close packed structures, and uniformly expand the crystal to lower densities in small steps. At each density, we use cell theory to calculate the free energy. In Fig. 3.8 we plot the results obtained for FCC, BCC and BCT with $\beta\epsilon = 1.0$ and $\delta = 0.15$. Here we observe that for each structure the free energy can be divided into three curves. Each of these curves correspond to a different behavior of the energy within the cell. For example, for the case of FCC, in the high density regime ($1.12 \lessapprox \rho\sigma^3 < \sqrt{2}$), the particle interacts with all 12 of its nearest neighbors, regardless of its position in the cell. This corresponds to the close packed FCC phase. For slightly smaller densities ($\sqrt{2}/[(\sigma+\delta)/\sigma]^3 < \rho\sigma^3 \lessapprox 1.12$), the particle interacts with 12 neighbors in its central position in the cell, but can lower its energy by deviating from the center. In this regime, cell theory is expected to break down, since the particle will preferentially sit at the edges of its cell. This conflicts with the cell theory assumption that all particles are, on average, found at their ideal lattice position. As a result, we do not include this regime in our stability analysis. Finally, in the density regime $0.53 \lessapprox \rho\sigma^3 < \sqrt{2}/[(\sigma+\delta)/\sigma]^3$, the particle interacts with none of its neighbors when it is inserted at its lattice site. This corresponds to the $FCC + \delta$ structure. Similar regimes occur for the other crystal structures. However, since the low-density branches of the BCC and BCT free energies are always less stable than the $FCC + \delta$ structure, we only need to consider the highest-density branch for these phases.

In the plot for FCC, Fig. 3.8a we added the density of close-packed FCC and $FCC+\delta$. In calculating the stability we only consider the two outer curves left of both FCC and $FCC+\delta$ lines. In Fig. 3.8b the free energy of the BCC structure is plotted with its theoretical density maximum density. For BCC we consider only the curve with the highest density in calculating its stability. In the case of the BCT, Fig. 3.8c structure there is no known theoretical density therefore we use the density found with the FBMC simulations. Also for BCT we only consider the curve with the highest density in calculating its stability. For each $\beta\epsilon \in \{0.5, .., 5.0\}$ we fit these curves to calculate obtain expressions for the free energy as function of the density.

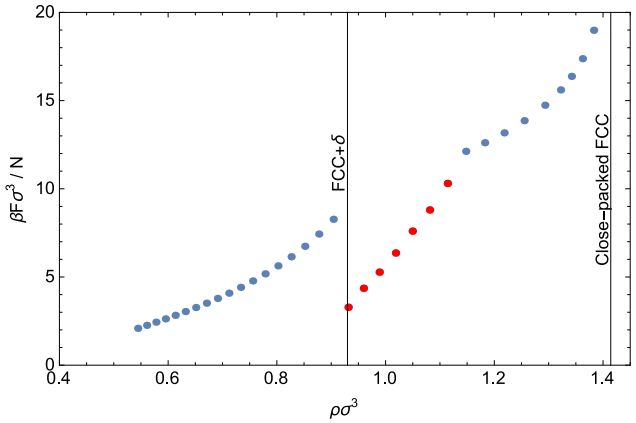

(a) Free energy FCC structure.

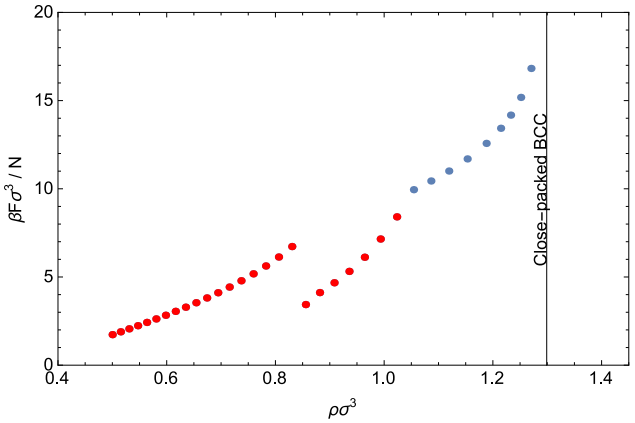

(b) Free energy BCC structure.

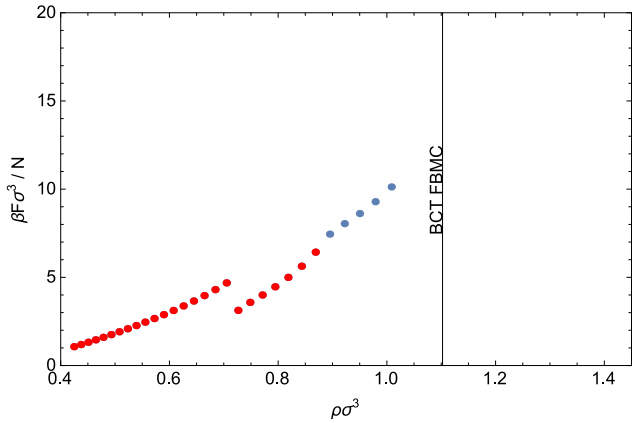

(c) Free energy BCT structure.

Figure 3.8: Free energy for different densities calculated using cell theory with square shoulder potential $\beta\epsilon = 1.0$ and shoulder length $\delta/\sigma = 0.15$. FCC (a), BCC (b) and BCT structures (c) are devided in three different curves. Only curves with blue points are considered in our stability analysis. The theoretical values of the density of FCC, $FCC+\delta$ and BCC are added (vertical black line). For the BCT structure the highest density found in the FBMC simulations is added.

3.2.3 Common tangent

To calculate the stability of crystal structures we plot the free energy per volume as a function of the density for both the fluid and the crystal structures. To illustrate this, in Fig. 3.9 we plot the free energies per volume for $\beta\epsilon = 1.0$ and $\delta/\sigma = 0.15$. Here, we see that both $FCC + \delta$ and BCT have higher free energies than the fluid, BCC and FCC phase. At $\beta\epsilon = 1.0$ both structures are therefore not stable. In this representation we can construct a common tangent between two phases to calculate the coexistence between these structures. By construction, these common tangents connect the densities at which the two phases have the same pressure and chemical potential. At any given density, the phase or coexistence with the lowest free energy is stable. Hence, for $\beta\epsilon = 1.0$ there is a coexistence between the fluid and BCC phase and between the BCC and FCC phase, as we can see from the common tangents in Fig. 3.10.

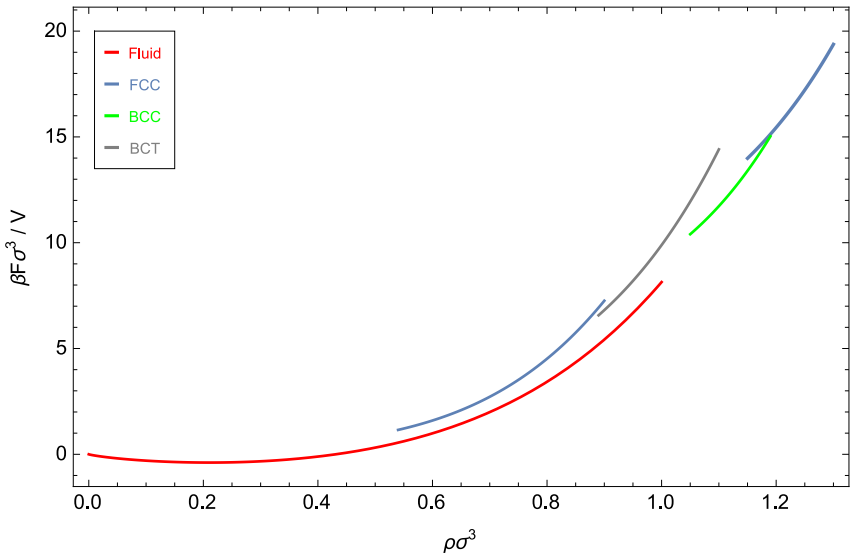

Figure 3.9: Free energy per volume as function of the density for the fluid phase (red) and the crystal structures FCC (blue), BCC (green) and BCT (gray) with $\beta\epsilon = 1.0$ and $\delta/\sigma = 0.15$.

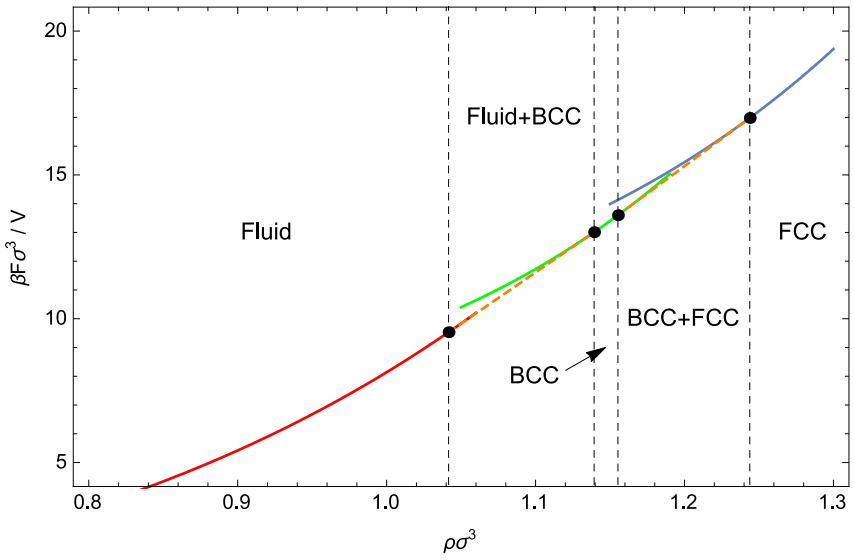

Figure 3.10: Common tangents between a fluid and BCC, and between BCC and FCC with $\beta\epsilon = 1.0$ and $\delta/\sigma = 0.15$. Between two black dots there is coexistence between the phases. Stable regions are added and separated by the black dashed lines.

In Fig. 3.11 we illustrate all stable phase transitions for shoulder length $\delta/\sigma = 0.15$. For sufficiently weak interactions ($\beta\epsilon \lessapprox 0.75$), the BCC structure becomes unstable as we can see from Fig. 3.11a. Here the free energy per volume of BCC is just above the common tangent between the fluid and FCC phase. If we increase the interaction strength to $\beta\epsilon = 2.5$ $FCC + \delta$ becomes stable, as see in Fig. 3.11b. Here the free energy of $FCC + \delta$ crosses the free energy of the fluid phase. As the free energy of the fluid phase is lower than the common tangent between $FCC + \delta$ and BCC we have a re-entrant phase transition of the fluid phase. Above $\beta\epsilon = 3.0$ the higher density fluid phase become unstable en is replaced by the BCT phase. This can be seen in Fig. 3.11c where the free energy of the fluid phase is slightly higher than the common tangent between the $FCC + \delta$ and BCT phase. We can combine the results for all investigated choices of $\beta\epsilon \in \{0.5, ..5.0\}$ to construct a phase diagram for a fixed shoulder length δ.

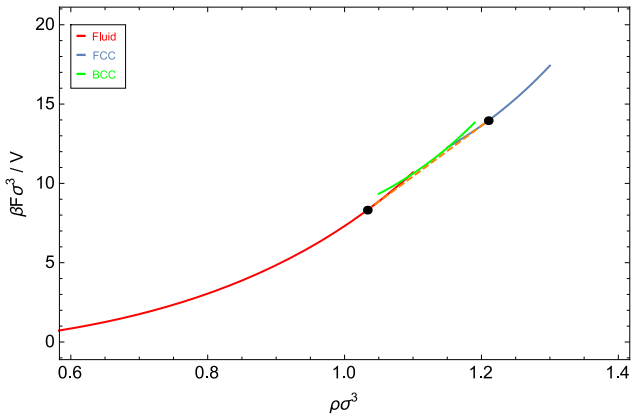

(a) Free energies $\beta\epsilon = 0.75$.

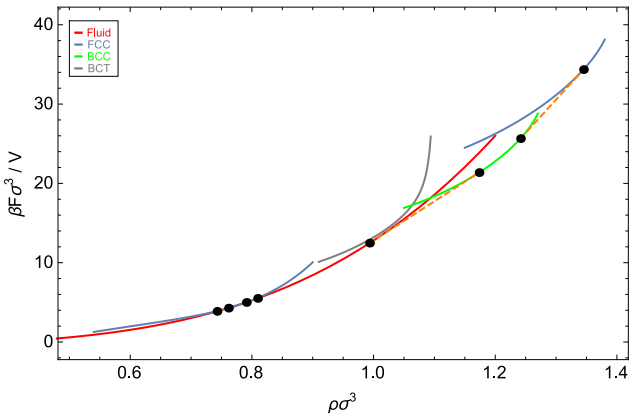

(b) Free energies $\beta\epsilon = 2.5$.

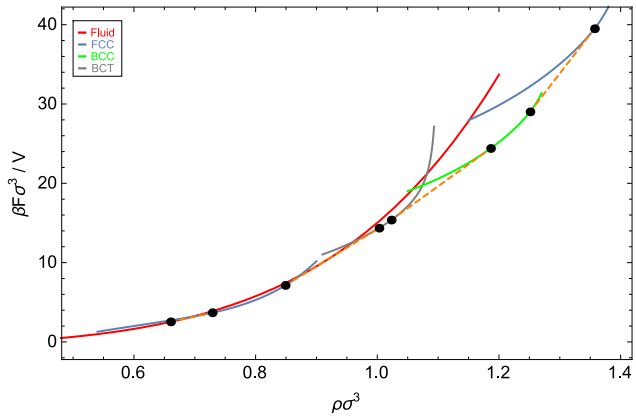

(c) Free energies $\beta\epsilon = 3.0$.

Figure 3.11: Free energy calculations of fluid and solid phases. For $\beta\epsilon = 1.0$ (a) a common tangent between the fluid and FCC free energy curve is plotted. Here we observe that the BCC free energy curve is just above this common tangent. For $\beta\epsilon = 2.5$ (b) the free energy of $FCC + \delta$ crosses the fluid curve whereas the BCT free energy is higher than the common tangent between the fluid and BCC curve. In (c) all common tangents between fluid and solids are plotted for $\beta\epsilon = 3.0$.

3.2.4 Phase diagram

A phase diagram depicts the limits of stability for the stable phases. Here we are interested in the stability for the variables k_BT/ϵ as function of the reduced density $\rho\sigma^3$. The coexistence between two phases provide the limits for the different phases. In Fig. 3.12 we combined all common tangents for $\delta = 0.15$ as calculated in Sec. 3.2.3. By choosing the the vertical axis as k_BT/ϵ we can include the low temperature limits found in literature and from the FBMC simulations. In the phase diagram there are 5 different stable phases, the fluid, $FCC + \delta$, BCC, BCT and FCC phase. In the low temperature limit all 5 phases are stable. For a system with square shoulder potential the internal energy is determined by the number of bonds. Due to entropy, only the structure with the highest possible density per number of bonds will be stable. Here these are BCT with 4, BCC with 8 and FCC with 12 bonds per particle that have the highest entropy and thus the lowest free energy. If we increase the temperature first the BCT structure will melt at $k_BT/\epsilon \approx 0.35$. At $k_BT/\epsilon \approx 0.4$ the BCT phase is replaced by a more stable fluid phase. Here, a re-entrant phase transition of the fluid phase occurs as it is stable in two density regions. The $FCC + \delta$ phase melts at $k_BT/\epsilon \approx 0.41$, above this temperature the fluid phase has a large stable region up to a density of $\rho\sigma^3 \approx 1.0$. Above $k_BT/\epsilon \approx 1.2$ the BCC phase also melts leaving only a stable fluid and FCC phase.

Although, we are still in the process of analyzing, there is an absence of the crystal structures found for square shoulder length $\delta = 0.20$, we predict a partial phase diagram using only the structures $FCC + \delta$, BCC and FCC. Although the BCC structure was not found to be stable at the low temperature limit we still test its stability at higher temperatures. In Fig. 3.14 we see that BCC is still absent. At $\rho\sigma^3 \approx 0.3$ the fluid phase is stable at of two densities regions which is lower than for $\delta = 0.15$. Above $\rho\sigma^3 \approx 0.3$ the $FCC + \delta$ crystal melts and only the fluid and FCC phase are stable. Additional calculations on the free energy of the crystals found in the FBMC simulations could still change the phase diagram.

In 1997 Rascon et. al [14] predicted a phase diagram using density-functional perturbation theory for particles with a square shoulder potential. Here they find stable regions for both $FCC+\delta$, FCC and BCC at shoulder length $\delta = 0.16$, see Fig. 3.13a. The region for FCC and $FCC + \delta$ match that in Fig. 3.12. However, as already suggested by the authors, the stability of the BCC phase is strongly overestimated. In a more recent study by Fomin et al. [25] the $FCC + \delta$, BCC and FCC structure were predicted at low temperatures using a smoothed version of the square shoulder potential. Like in the phase diagram of Rascon et al. the BCT structure is absent, see Fig. 3.13b. The free energy of the crystals was calculated by thermodynamic integration to an Einstein crystal. Both the $FCC + \delta$ and BCC structure melt at a lower temperature, $k_BT/\epsilon \approx 0.35$ and $k_BT/\epsilon \approx 0.9$ respectively. These discrepancies can likely be attributed to the smoothening of the potential, which results in a significantly less pronounced shoulder.

More recently, Ziherl and Kamien [15] theoretically predicted the phase diagram for a system with a square shoulder potential. In particular, they made use of a self-consistent mean-field theory which attempts to partially incorporate the fluctuations of the particles around their ideal lattice site. The fluid phase was not considered, except by assuming that the zero-temperature coexistence with $FCC + \delta$ will remain valid at higher temperatures. For the phase diagram with square shoulder length $\delta/\sigma = 0.20$, see Fig. 3.15. Taking into account the fluid phase, and using the cell theory described in Sec. 2.4.2, we thus far do not find stable regions for the $A15$ and BCC phases. Instead, we observe a significant increase in the stability of the fluid phase at temperatures above zero, as well as a large variation of additional crystal structures stable in the low temperature regime. Identification and stability analysis of these additional structures is still ongoing.

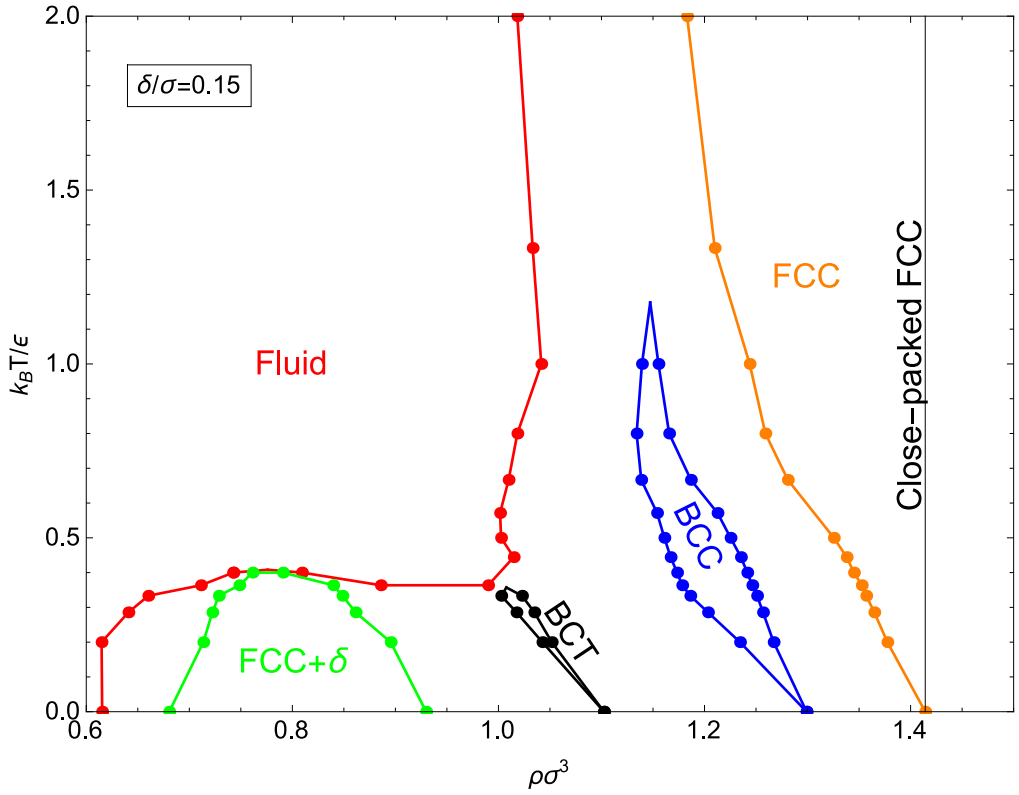

Figure 3.12: Phase diagram for square shoulder potential with shoulder length $\delta/\sigma = 0.15$. There are 5 stable regions, the fluid, $FCC + \delta$, BCC, BCT and FCC phase. The close-packed FCC structure is indicated by the vertical black line. Lower temperature limits are provided by literature and FBMC simulations. Finite temperature results calculated with free energy approximations using cell theory for the solid phases and thermodynamic integration of the fluid phase.

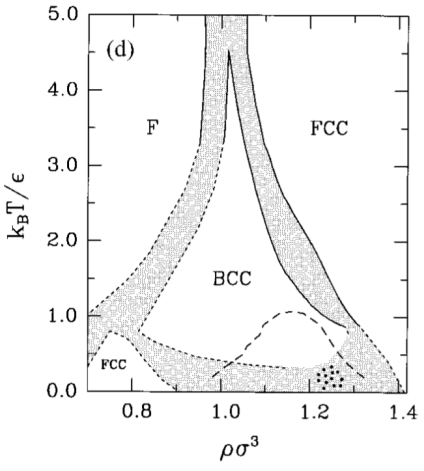

(a) Phase diagram predicted by Rascon et. al [14] for $\delta/\sigma = 0.16$.

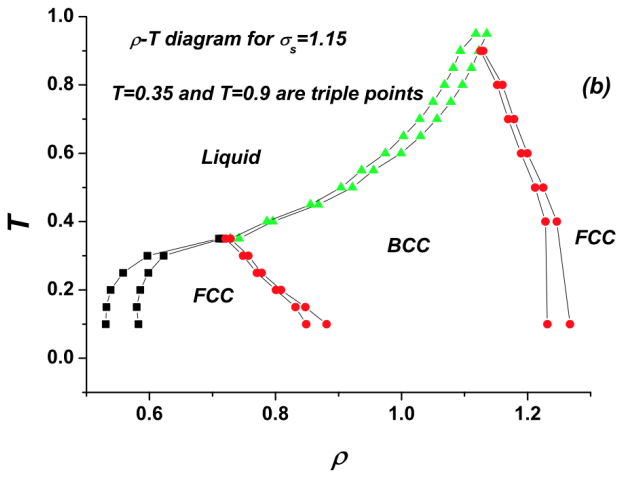

(b) Phase diagram predicted by Fomin et al. [25] for $\delta/\sigma = 0.15$.

Figure 3.13

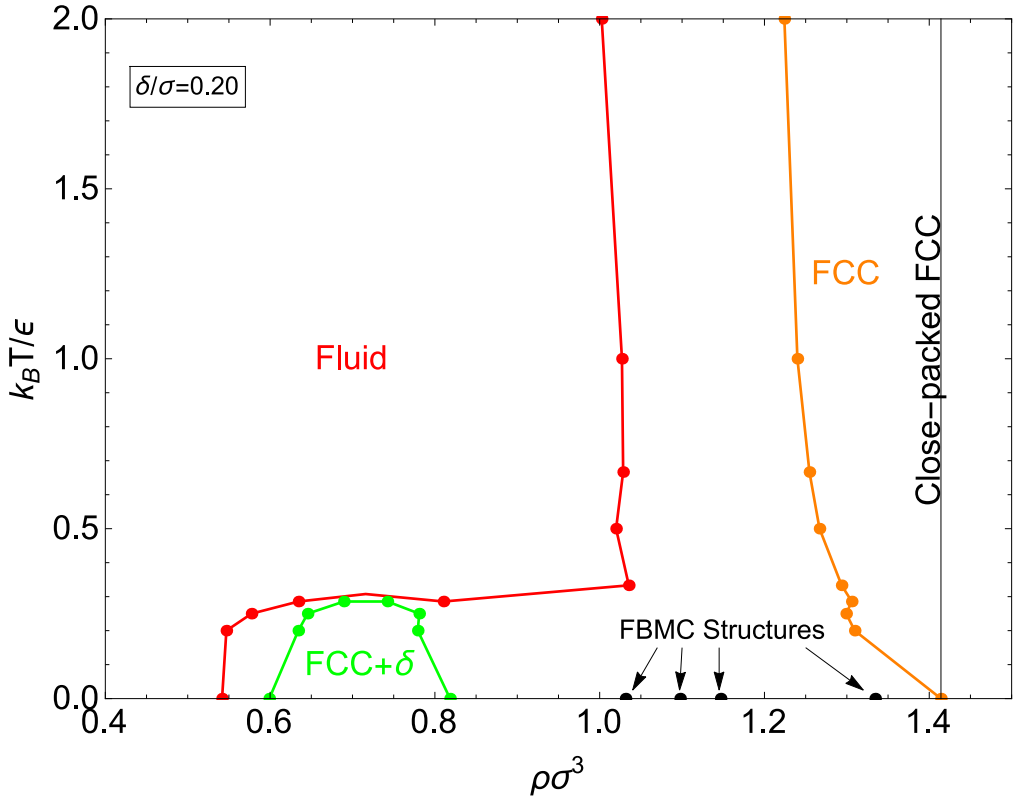

Figure 3.14: Partial phase diagram for square shoulder potential with shoulder length $\delta/\sigma = 0.20$. There are 3 stable regions, the fluid, $FCC + \delta$ and FCC phase. The close-packed FCC structure is indicated by the vertical black line. Lower temperature limits are provided by literature. Finite temperature results calculated with free energy approximations using cell theory for the solid phases and thermodynamic integration of the fluid phase. Results from the FBMC simulation are added.

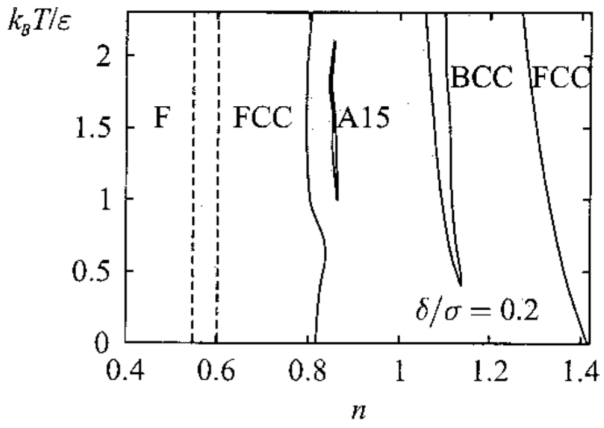

Figure 3.15: Phase diagram predicted by Ziherl and Kamien [15] for $\delta/\sigma = 0.20$.

4 Conclusion and discussion

The self-assembly of NPs into complex structures, such as the $MgZn_2$ structure [2], can often be understood with fairly simple interactions. To better understand how these structures are formed we need to closely examine the interactions between these particles. Here we explored whether the emergence of this structure can be explained by a simple model for their interaction potential, the square shoulder model. For this we have successfully implemented the floppy-box Monte Carlo (FBMC) method to predict crystal structures. In the low temperature limit we found $FCC + \delta$, BCC, BCT and FCC to be stable for a square shoulder potential with shoulder length $\delta/\sigma = 0.15$. For shoulder length $\delta/\sigma = 0.20$ we classified 4 new crystal structures based on their planar structures and energy contribution. For the potential stable crystal structures in the low temperature limit we calculated their approximate Helmholtz free energy using cell theory. To fully determine their stability, we also calculated the free energy of the fluid phase using thermodynamic integration of the equation of state. With these results we predicted a phase diagram. For $\delta/\sigma = 0.15$ there are 5 stable regions, the fluid, $FCC + \delta$, BCC, BCT and FCC phase. Calculating the free energy of the newly classified crystal structures found for $\delta/\sigma = 0.20$ is still ongoing. Therefore, only a partial phase diagram was predicted where we found a stable fluid, $FCC + \delta$ and FCC phase. Additional free energy calculations of the found crystal structures for $\delta/\sigma = 0.20$ could therefore still alter the phase diagram.

Our work shows that the simple square-shoulder potential can form a large variety of different crystal structures in the investigated regime of interaction ranges. This includes several structures which had not previously been reported or considered for this model. In the near future, we will complete the zero temperature phase diagram for a larger range of shoulder length δ. As we did not find a stable $MgZn_2$ structure, future research should look into modifications to this model which could stabilize this experimentally found structure. For this, one could look into polydispersity, softness of the shoulder, and many-body interactions. When considering these options, knowledge of the stable structures in a square-shoulder system is an important starting point.

References

[1] J. Schmitt, S. Hajiw, A. Lecchi, J. Degrouard, A. Salonen, M. Impéror-Clerc, and B. Pansu, *Formation of superlattices of gold nanoparticles using ostwald ripening in emulsions: Transition from fcc to bcc structure*, The Journal of Physical Chemistry B **120**, 5759 (2016).

[2] S. Hajiw, B. Pansu, and J.-F. Sadoc, *Evidence for a c14 frank–kasper phase in one-size gold nanoparticle superlattices*, ACS Nano **9**, 8116 (2015).

[3] L. Filion, M. Marechal, B. van Oorschot, D. Pelt, F. Smallenburg, and M. Dijkstra, *Efficient method for predicting crystal structures at finite temperature: variable box shape simulations*, Physical Review Letters **103**, 188302 (2009).

[4] R. Brown, *Xxvii. a brief account of microscopical observations made in the months of june, july and august 1827, on the particles contained in the pollen of plants; and on the general existence of active molecules in organic and inorganic bodies*, Philosophical Magazine Series 2 **4**, 161 (1828).

[5] J. Prost, *The physics of liquid crystals* (Oxford University Press, 1995).

[6] G. W. Scherer and J. C. Luong, *Glasses from colloids*, Journal of Non-Crystalline Solids **63**, 163 (1984).

[7] W.-H. Shih, W. Y. Shih, S.-I. Kim, J. Liu, and I. A. Aksay, *Scaling behavior of the elastic properties of colloidal gels*, Physical Review A **42**, 4772 (1990).

[8] A. Denton and H. Löwen, *Stability of colloidal quasicrystals*, Physical Review Letters **81**, 469 (1998).

[9] B. De Nijs, S. Dussi, F. Smallenburg, J. D. Meeldijk, D. J. Groenendijk, L. Filion, A. Imhof, A. Van Blaaderen, and M. Dijkstra, *Entropy-driven formation of large icosahedral colloidal clusters by spherical confinement*, Nature Materials **14**, 56 (2015).

[10] W. H. Evers, B. D. Nijs, L. Filion, S. Castillo, M. Dijkstra, and D. Vanmaekelbergh, *Entropy-driven formation of binary semiconductor-nanocrystal superlattices*, Nano Letters **10**, 4235 (2010).

[11] A. Denton and H. Löwen, *Isostructural solid-solid transitions in square-shoulder systems*, Journal of Physics: Condensed Matter **9**, L1 (1997).

[12] G. J. Pauschenwein and G. Kahl, *Clusters, columns, and lamellae—minimum energy configurations in core softened potentials*, Soft Matter **4**, 1396 (2008).

[13] H. Pattabhiraman, A. P. Gantapara, and M. Dijkstra, *On the stability of a quasicrystal and its crystalline approximant in a system of hard disks with a soft corona*, The Journal of Chemical Physics **143**, 164905 (2015).

[14] C. Rascón, E. Velasco, L. Mederos, and G. Navascués, *Phase diagrams of systems of particles interacting via repulsive potentials*, The Journal of Chemical Physics **106**, 6689 (1997).

[15] P. Ziherl and R. D. Kamien. *Maximizing entropy by minimizing area: Towards a new principle of self-organization*, (2001).

[16] N. Metropolis, A. W. Rosenbluth, M. N. Rosenbluth, A. H. Teller, and E. Teller, *Equation of state calculations by fast computing machines*, The Journal of Chemical Physics **21**, 1087 (1953).

[17] D. Frenkel, B. Smit, J. Tobochnik, S. R. McKay, W. Christian, et al., *Understanding molecular simulation*, Computers in Physics **11**, 351 (1997).

[18] S. Prestipino, F. Saija, and G. Malescio, *The zero-temperature phase diagram of soft-repulsive particle fluids*, Soft Matter **5**, 2795 (2009).

[19] J. Lennard-Jones and A. Devonshire, *Critical phenomena in gases. i*, Proceedings of the Royal Society of London. Series A, Mathematical and Physical Sciences (1937).

[20] P. J. Steinhardt, D. R. Nelson, and M. Ronchetti, *Bond-orientational order in liquids and glasses*, Physical Review B **28**, 784 (1983).

[21] Y. Wang, S. Teitel, and C. Dellago, *Melting of icosahedral gold nanoclusters from molecular dynamics simulations*, The Journal of Chemical Physics **122**, 214722 (2005).

[22] P. Rein ten Wolde, M. J. Ruiz-Montero, and D. Frenkel, *Numerical calculation of the rate of crystal nucleation in a lennard-jones system at moderate undercooling*, The Journal of Chemical Physics **104**, 9932 (1996).

[23] S.-C. Mau and D. A. Huse, *Stacking entropy of hard-sphere crystals*, Physical Review E **59**, 4396 (1999).

[24] R. Dunlap, *The symmetry and packing fraction of the body centered tetragonal structure*, European Journal of Physics Education **3**, 19 (2012).

[25] Y. D. Fomin, N. Gribova, V. Ryzhov, S. Stishov, and D. Frenkel, *Quasibinary amorphous phase in a three-dimensional system of particles with repulsive-shoulder interactions*, The Journal of Chemical Physics **129**, 064512 (2008).

[26] T. C. Hales, *The sphere packing problem*, Journal of Computational and Applied Mathematics **44**, 41 (1992).

[27] D. Frenkel, *Entropy-driven phase transitions*, Physica A: Statistical Mechanics and Its Applications **263**, 26 (1999).